Ultrafast negative thermal expansion driven by spin disorder

J. Pudell,[1] A. von Reppert,[1] D. Schick,[2,3] F. Zamponi,[1] M. Rössle,[1,3] M. Herzog,[1] H. Zabel,[4] and M. Bargheer[1,3,*]

[1]*Institut für Physik und Astronomie, Universität Potsdam, Karl-Liebknecht-Strasse 24-25, 14476 Potsdam, Germany*

[2]*Max-Born-Institut Berlin, Max-Born-Straße 2a, 12489 Berlin, Germany*

[3]*Helmholtz Zentrum Berlin, Albert-Einstein-Strasse 15, 12489 Berlin, Germany*

[4]*Fakultät für Physik und Astronomie, Ruhr-Universität Bochum, 44780 Bochum, Germany*

(Received 27 July 2018; revised manuscript received 15 February 2019; published 11 March 2019)

We measure the transient strain profile in a nanoscale multilayer system composed of yttrium, holmium, and niobium after laser excitation using ultrafast x-ray diffraction. The strain propagation through each layer is determined by transient changes in the material-specific Bragg angles. We experimentally derive the exponentially decreasing stress profile driving the strain wave and show that it closely matches the optical penetration depth. Below the Néel temperature of Ho, the optical excitation triggers negative thermal expansion, which is induced by a quasi-instantaneous contractive stress and a second contractive stress contribution increasing on a 12-ps timescale. These two timescales were recently measured for the spin disordering in Ho [Rettig *et al.*, Phys. Rev. Lett. **116**, 257202 (2016)]. As a consequence, we observe an unconventional bipolar strain pulse with an inverted sign traveling through the heterostructure.

DOI: 10.1103/PhysRevB.99.094304

I. INTRODUCTION

In most of the research on ultrafast magnetism the lattice was considered only as an angular momentum sink [1–3]. Ultrafast effects on the lattice induced by demagnetization have been discussed surprisingly rarely [4–7]. Time-resolved magneto-optical Kerr measurements and optical picosecond ultrasonics are the workhorse for many researchers [1,2,8–12]. Ultrafast electron diffraction (UED) or ultrafast x-ray diffraction (UXRD) experiments that directly observe the transient lattice strain induced by ultrafast demagnetization have been discussed only sporadically [4,5,13–15]. Several ultrafast diffraction studies on the transition metals Ni and Fe [16–18] discuss the strain waves excited by electron and phonon stresses σ_e and σ_{ph}, and theory predicts relevant electron-phonon (e-ph) coupling constants [19] even with mode specificity [20]. Very recently, granular FePt films were studied by UXRD [21] and UED [5]. The rapid out-of-plane lattice contraction could be convincingly ascribed to changes in the tetragonality of the lattice by *ab initio* calculations of the total ground-state energy for the spin system in the paramagnetic and ferromagnetic phases [5]. To simulate the dynamic changes in a system with several degrees of freedom it is common to apply multiple-temperature models [5,9] which assume that each subsystem can be described by an individual temperature T_i, although it has been shown that different phonon modes may be out of thermal equilibrium for 100 ps [20]. Specialized techniques allow for assigning timescales to specific electronic processes and orbitals or bands [3,22–25]. This is particularly relevant in the magnetic rare earths, where the exchange interaction between the localized $4f$ spin and orbital magnetic moments is mediated by the itinerant $5d6s$ conduction electrons via the Ruderman–Kittel–Kasuya–Yosida (RKKY) interaction [26,27]. In antiferromagnetically ordered phases the question of angular momentum transfer is less relevant since the net magnetization is zero. Rare-earth elements prove to be a versatile testing ground for understanding how rapidly ultrafast demagnetization leads to stress in the crystal lattice. We selected Ho since a recent resonant hard x-ray scattering experiment measured that the demagnetization of both the localized $4f$ moments and the itinerant conduction electrons proceed on a fast 200-fs timescale attributed to electron-spin interaction and a slow 9-ps timescale for coupling phonons to the spins [22].

In this paper we use UXRD at a laser-based femtosecond plasma x-ray source (PXS) to show that the ultrafast laser excitation of Ho below its Néel temperature $T_N = 132\,\mathrm{K}$ generates negative stress that rises on the two timescales for disordering the spin system [22] and drives bipolar strain wave packets with an inverted sign compared to common materials without negative thermal expansion (NTE) [8,28]. We use the material specificity of UXRD to cross-check the individual lattice constant changes in this metallic multilayer system, which is opaque to optical probes.

In the paramagnetic (PM) phase of Ho, the analysis is simplified by the complete spin disorder, and we show that the spatial excitation profile of the driving stress can be derived by probing the bipolar strain pulse in the adjacent Y and Nb buffer layers. The spatial stress profile is approximately given by the penetration depth of the pump pulses. The UXRD experiment in the antiferromagnetic (AFM) phase reveals an instantaneous compensation of the expansive electron and phonon stress in Ho by the negative instantaneous stress component $\sigma_{sp,0}$ due to spin disorder. In addition to this subpicosecond negative-stress component, the negative stress $\sigma_{sp}(t)$ keeps rising on a 12-ps timescale. These negative-stress

*bargheer@uni-potsdam.de; http://www.udkm.physik.uni-potsdam.de

components in Ho are evidenced in the adjacent Y and Nb by the extended leading expansive edge of the propagating bipolar strain pulse, which has an opposite sign compared to excitation of Ho in the PM phase. Thus, we observe dynamic stress rising on the two timescales on which disordering of the spin helix was observed by resonant x-ray scattering [22]. However, we emphasize that the observed lattice contraction in Ho is about 20 times larger than the peak shift of the magnetic Bragg peak that was observed for very similar fluence [22] because it, in fact, measures the period of spin helix which is incommensurate with the lattice.

In a broader context, our observation of ultrafast lattice contraction in Ho is discussed as an example of a rapid entropy-driven manifestation of the NTE phenomenon, which may occur on different timescales in various materials ranging from nonmagnetic molecular nanocrystals [29] and oxides with open oxygen frameworks [30] to ferroelectrics [31] and magnetically ordered systems like Heusler alloys [32].

II. SPIN-GRÜNEISEN CONSTANT AND NTE

In laser-excited magnetic systems, the role of a nonequilibrium within and/or among the different subsystems is heavily debated. The prevalent basis of the discussions is multiple-temperature models. In thermal equilibrium, standard thermodynamic approaches emphasize the role of the entropy S by calculating the equilibrium lattice constants from the minimum of the Gibbs free energy $G = U + pV - TS$ [33,34]. For a discussion of lattice dynamics, where the change in volume V is driven by a pressure p or, for an anisotropic case, the strain ε is driven by a stress σ, we can circumvent the discussion of a (non)equilibrium temperature by considering the energy density ρ^Q.

It is common to evoke the macroscopic Grüneisen coefficients (GCs) $\Gamma_{\mathrm{e,ph}}$ for phonons and electrons, which describe the efficiency of generating stress $\sigma_{\mathrm{e,ph}} = \Gamma_{\mathrm{e,ph}} \rho^Q_{\mathrm{e,ph}}$ by a heat energy density $\rho^Q_{\mathrm{e,ph}}$ [34]. If $\Gamma_{\mathrm{e}} \neq \Gamma_{\mathrm{ph}}$, ultrafast diffraction allows inferring the time-dependent $\sigma(t)$ from the observed transient strain $\varepsilon(t)$ [16,17,35]. Hooke's law relates ε linearly to σ and hence to the energy densities $\rho^Q_{\mathrm{e,ph}}$ deposited in each subsystem. The Grüneisen concept was extended to stress resulting from spin excitations in Ni and Fe [33,36], but the experimental verification remained ambiguous [16–18]. Thermodynamic analysis affirms that the GCs generally measure how entropy S depends on strain ε [37]. While for a gas of phonons or electrons the entropy usually increases with the volume, the phenomenon of NTE generally occurs when the entropy S decreases upon expansion, i.e., $\partial S/\partial \varepsilon < 0$. There are various origins of NTE [33,34]; however, for spin-ordered phases of rare earths, the NTE along the c axis of the hexagonal lattice is very large and clearly associated with the energy density ρ^Q_{sp} of the spin system. Figure 1(a) shows the three contributions $C_{\mathrm{e,ph,sp}}(T)$ to the specific heat [38,39]. The negligible contribution of the electron system is barely visible as a gray area below the red shaded phonon contribution. The blue shaded spin contribution is very large for all temperatures below T_{N}, and close to the second-order phase transition to the PM phase it is even larger than the phonon contribution. Figure 1(b) indicates the change in the c-axis lattice constant, which is negative, when the spin contribution

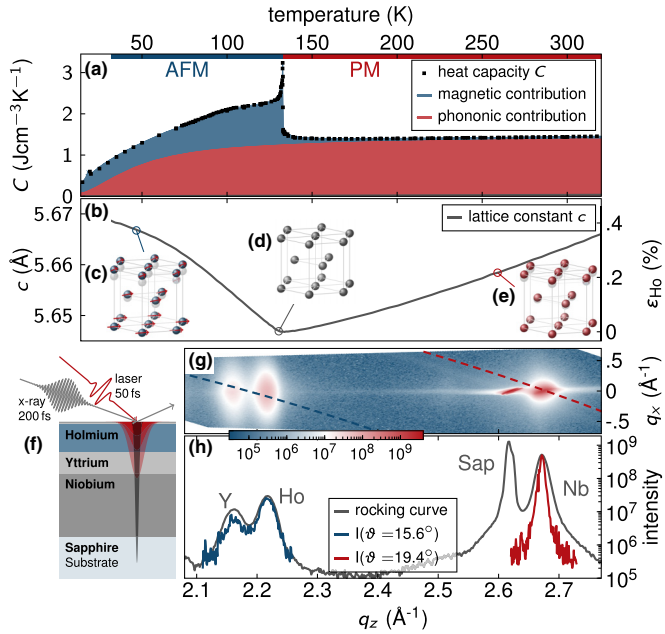

FIG. 1. (a) Specific heat of Ho [38,39] separated into the three contributions $C_{\mathrm{e,ph,sp}}(T)$, where the electron contribution $C_{\mathrm{e}}(T)$ is hardly visible and the spin contribution C_{sp} even exceeds the phonon contribution C_{ph} at some temperatures. (b) c axis of the Ho thin film as a function of temperature, showing large NTE below $T_{\mathrm{N}} = 132$ K. (c)–(e) Schematics of the hexagonal lattice illustrating the c-axis lattice change and the helical spin order below T_{N}. (f) Schematic of the layer stacking and the pump-probe geometry. (g) The RSM including separated Bragg peaks of Y, Ho, sapphire, and Nb. The slices of the RSM used for (h) and the time-resolved measurements are shown in red (Nb) and blue (Ho+Y). (h) The projection of the full RSM (gray) and measurements along the slices with a fixed angle ω (red and blue).

to the specific heat is large. Surprisingly, also in these systems exhibiting a divergent specific heat at the phase transition, the spin GC Γ_{sp} is essentially independent of T [13,14], even though the total GC [37] varies strongly with T. Separating phonon and spin contributions to the thermal expansion and the heat capacity of Ho yields $\Gamma_{\mathrm{ph}}/\Gamma_{\mathrm{sp}} \approx -0.2$ [33,37]. This implies that equal energy densities in the spin and phonon system lead to a five times larger contractive stress, which overwhelms the expansive phonon stress. The separate GC $\Gamma_{\mathrm{e,ph,sp}}$ are independent of T because the T dependences of the specific heat $C_{\mathrm{e,ph,sp}}(T)$ and the thermal expansion coefficient $\alpha_{\mathrm{e,ph,sp}}(T)$, which originate from the quantum nature of the excitations, cancel out [33,34]. This linear dependence of energy density and stress in each subsystem makes the Grüneisen concept useful and causes temperature and thermal equilibrium within each subsystem to be properties of secondary relevance to the dynamics. Nonetheless, the temperature-dependent specific heats $C_{\mathrm{e,ph,sp}}(T)$ map the multiple-thermal energy model onto classical multiple-temperature models.

III. EXPERIMENTAL DETAILS

The multilayer stack was grown by molecular beam epitaxy on sapphire in the sequence 128 nm Nb, 34 nm Y,

46 nm Ho with a thin capping layer of 4 nm Y and 3 nm Nb [see Fig. 1(f)]. X-ray reflectivity measurements confirm the total thickness of the metallic multilayer on the sapphire substrate; 200-fs hard x-ray probe pulses with a photon energy of 8 keV are derived from the PXS at the University of Potsdam [40]. The *p*-polarized 50-fs laser pulses with a diameter of 1500 μm (FWHM) excite the sample at an incidence angle of about 52°. The incident fluence of the 800-nm pump pulses is 3 mJ/cm^2; an absorbed fluence of 1.7 mJ/cm^2 is calculated according to the refractive index obtained by spectroscopic ellipsometry. The penetration depth is 21 nm at 800 nm for all temperatures. A schematic of the sample and the pump-probe geometry is given in Fig. 1(f).

The reciprocal space map (RSM) of the multilayer system including separated Bragg peaks of Y, Ho, sapphire, and Nb at room temperature is shown in Fig. 1(g). The map is obtained by recording the symmetrically and asymmetrically diffracted x rays on the area pixel detector (Dectris PILATUS 100K) as a function of the "rocking" angle ω between the sample surface and the center of the convergent femtosecond x-ray beam [40]. The gray line in Fig. 1(h) shows a projection of the full RSM onto the out-of-plane component q_z. The red and blue lines indicate typical x-ray diffraction curves derived from the dashed cuts through reciprocal space indicated by the red and blue lines in Fig. 1(g). These cuts are given by the x rays' angle of incidence ω chosen for the UXRD experiments. The center position of the Bragg reflection is obtained by fitting a Gaussian function to each layer peak.

IV. RESULTS

Figure 2 summarizes the strain in all three layers for the PM phase of Ho (red) and in the helical AFM phase of Ho around 40 K (blue). The individual data points were obtained by fitting a Gaussian function to each layer peak. In the PM phase two characteristic times are identified from the UXRD data: At $t = 17$ ps, Ho has reached the maximum expansion. This indicates the time it takes the expansive sound to travel from the surface to the Y interface. At this time the leading compressive part of the bipolar strain wave packet [8,28] has fully propagated from the Ho into the Y layer, as evidenced by the pronounced minimum in the Y strain (see Fig. 3 for an illustration of the strain wave). At $t = 26$ ps the zero crossing of the bipolar strain wave packet traverses the Y/Nb interface, which yields the pronounced minimum in the Nb strain. These characteristic time points yield the layer thicknesses given above.

The UXRD data recorded in the AFM phase of Ho directly show a delay of the contractive strain in Ho [Fig. 2(a), blue line]. The minimum of the Ho strain at about 23 ps is delayed by about 6 ps compared to the maximum in the PM phase. The signal in Y [Fig. 2(b)] confirms that also the propagating bipolar strain wave packet has a reversed sign of the strain amplitude at low temperature and a delay of about 6 ps. In the PM phase, the leading compressive part of the strain launched in Ho by thermal expansion reduces the out-of-plane lattice spacing in Y, although the Y layer is also excited by the pump pulse [28]. In the AFM phase the contractive stress in Ho dominates and reverses the sign of the bipolar

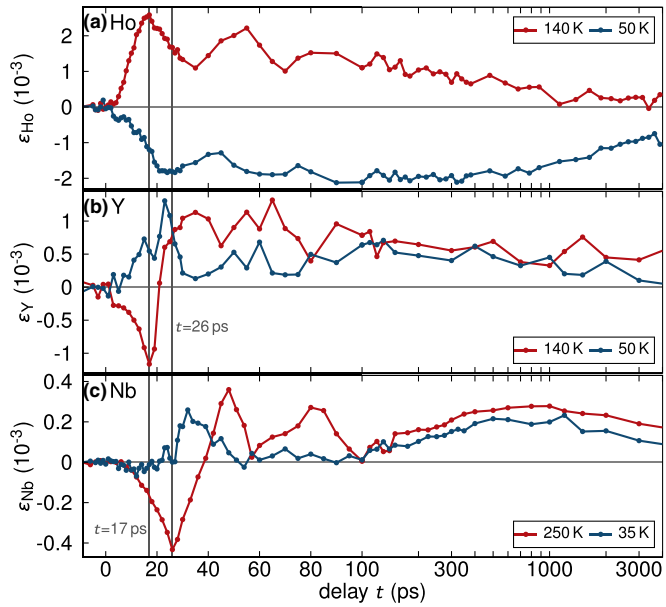

FIG. 2. Transient lattice strain ε for (a) Ho, (b) Y, and (c) Nb after laser excitation in the PM (red) and AFM (blue) phases as determined from UXRD. The thin solid line at 17 ps indicates the time it takes the maximum expansion starting at the surface to propagate to the Ho/Y interface. At this time Ho is maximally expanded, and Y is fully compressed since the expansive part of the bipolar strain is fully in the Ho layer, whereas the leading compressive part is only in the Y layer. The thin line at 26 ps indicates the same fully compressed situation for the Nb layer. In the AFM phase Ho [in (a)] has a 6-ps delay of the maximal contraction compared to the maximal PM expansion.

strain. Hence, the Ho contraction expands the adjacent Y, assisted by the small expansive stress from direct optical excitation of Y. The UXRD signal from the Nb layer is even cleaner, as a negligible amount of light is absorbed in this layer. Therefore, we repeated the experiments on Nb. The obtained signal [Fig. 2(c)] had to be scaled appropriately due to the slightly different base temperature and fluence. The tiny negative lattice constant change in Nb [Fig. 2(c)] in the first 15 ps is due to the stress generated in Y, and the crossover to the strong expansion starts around 10 ps, when the leading expansive part of the bipolar strain wave packet generated by the exponentially decaying compressive stress in Ho reaches the Nb layer. The very short wiggle of the average Nb layer strain at 26 ps heralds the rather strong but spatially narrow bipolar strain wave packet launched by the 7-nm-thick Nb/Y capping layer. The time perfectly coincides with the arrival of the wave created by surface expansion that was already observed in the PM phase. The same feature from the capping layer is also clearly observed in the Y data at 19 ps. In the PM data set, this feature is absent since the cap layer and the Ho layer both expand with similar amplitude.

For $t > 200$ ps the sound wave reflections have ceased, and we can safely interpret the expansion and contraction of each layer by the average energy densities $\rho_{e,ph,s}$. For earlier time delays, the spatially averaged thermal stress in each layer can be obtained from the data by averaging out the oscillations. For timescales shorter than the characteristic

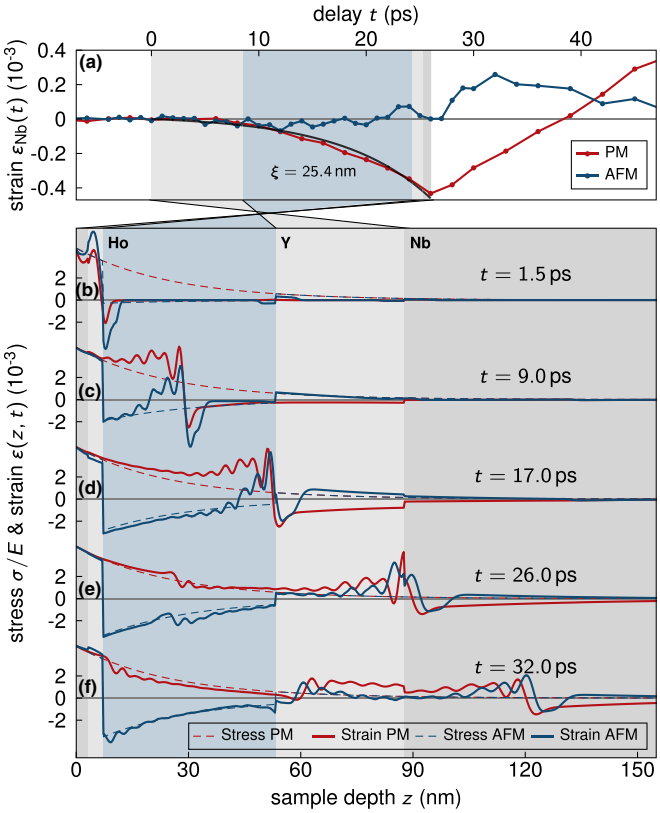

FIG. 3. (a) Zoom of the first 45 ps of the Nb data from Fig. 2(c). The black line shows an exponential fit to the strain in the PM phase, which is used to extract the driving stress via Hooke's law. (b)–(f) Stress (dashed) and strain profiles for selected delays in the heterostructure from a simulation. To avoid unimportant rapid oscillations in this graph, the temporal stress profile was smoothed by a 0.5-ps Gaussian function. The NTE stress in Ho rises with $\tau = 12$ ps. The inverted strain profile is most prominently seen in (c) and (d) in the Y and Nb layers, respectively. As an illustration, a video sequence of this temporal evolution of the stress profile and the strain wave is given in the Supplemental Material [41].

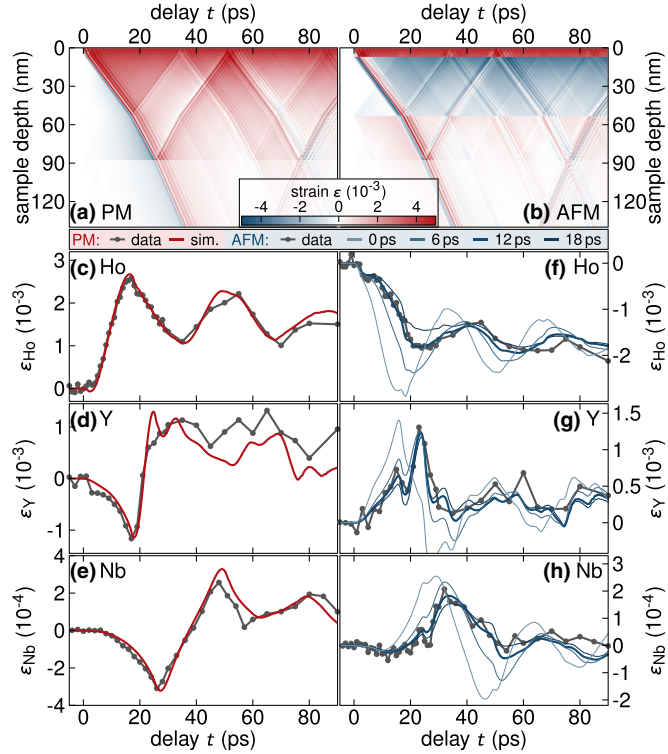

FIG. 4. The simulated spatiotemporal strain profiles show the traveling sound waves in the heterostructure in the (a) PM and (b) AFM phases. (c)–(e) Simulated strain for the PM phase in the three layers (red) is compared to the data. (f)–(h) Simulations for the AFM phase with varying time constant $\tau = 0$, 6, 12, and 18 ps. The best match to the data is obtained for $\tau = 12$ ps.

oscillation period of the layer, however, the transient stress must be obtained from modeling the elastic response of the system. The measured transient (negative) thermal expansion $\varepsilon(t) = \varepsilon_{th}(t) + \varepsilon_{sw}(t)$ is a linear superposition of the averaged thermal strain $\varepsilon_{th}(t)$ and the layer-averaged amplitude of the hypersound waves $\varepsilon_{sw}(t)$ triggered by the rapid expansion following the ultrashort pulse excitation, which reflect from the interfaces.

V. ANALYSIS

In this section we highlight the potential of UXRD for deriving the spatial form of the stress driving the observed strain [42,43]. In Fig. 3(a) we analyze the UXRD data recorded for the Nb layer in the PM state of Ho, zooming in on the pronounced compression signal of the Nb layer. The average strain ε_{Nb} shows an increasing compression slowly starting at $t = 0$ when the bipolar strain wave packet starts entering the Nb layer. Neglecting sound velocity differences in the heterostructure, an exponential spatial stress profile generates a bipolar strain pulse with a compressive leading edge that has an exponential spatial dependence as well [28].

Thus, from the measured strain in a dedicated detection layer, we can show that the spatial stress profile in fact decays exponentially with the characteristic length scale $\xi = 25$ nm which matches the value calculated from the optical constants measured by ellipsometry. For direct comparison with the data we plotted in Fig. 3(a) the stress $\sigma_{PM} = \sigma_0 e^{-z/\xi}$ onto the measured strain data using an appropriate scaling by Hooke's law. In the AFM phase (blue) the spin and phonon stress contributions approximately cancel out immediately after excitation. In Figs. 3(b)–3(f) we show the spatial stress profiles used in the further analysis of the data via simulations as dashed lines.

VI. MODELING AND DISCUSSION

Now we discuss the numerical modeling of the observed strain that is necessary to derive the transient stress changing faster than the characteristic thickness modulation time of the layers. In the PM phase of Ho we calculate the transient strain [Fig. 4(a)] by integrating the equation of motion for a linear masses-and-springs model using the UDKM1DSIM toolbox [44]. The experimentally derived exponential spatial form of the stress σ_{PM} serves as an input. Figures 4(c)–4(e) show the excellent agreement of the simulations with the measured data for all three layers in the PM phase when

using the exponentially decaying stress profile $\xi = 25$ nm derived above. For simplicity, we assume an instantaneous rise of the combined *e*-ph stress. Separate electron and phonon GCs do not improve the fit in Figs. 4(c)–4(e). We note that the energy density in each subsystem is linearly proportional to the stress and strain in each layer. The spatiotemporal strain shown in Fig. 4(a) is used as input parameter for the calculation of the x-ray diffraction pattern by dynamical x-ray diffraction theory. The positions of the simulated Bragg peaks are obtained by fitting a Gaussian function as done in the experimental data analysis. For illustration, Figs. 3(b)–3(f) depict the spatial strain profiles for selected time delays, which are cross sections of the spatiotemporal strain profiles in Figs. 4(a) and 4(b), leading to the fits in Fig. 4(c)–4(h). Figures 3(b)–3(f) contain the transient spatial stress profiles (dashed lines) used as input for the simulation. After about 30 ps [Figs. 3(e) and 3(f)] the simulated strain profile is very close to the simple stress-strain relation, with only a slight deviation due to residual hypersound waves. The observed signal oscillations (Fig. 4) due to hypersound waves reflected at the interfaces of all three layers are reproduced by the model.

To simulate the corresponding spatiotemporal strain [Fig. 4(b)] when Ho is excited in the AFM phase, we have to take into account the negative stress induced by spin disorder, which adds to the positive *e*-ph stress; the dynamics become richer and challenge the modeling. We model the transient stress $\sigma = \Gamma_{\text{e-ph}}\rho^{Q}_{\text{e-ph}} + \Gamma_{\text{sp}}\rho^{Q}_{\text{sp}}$ [Figs. 3(b)–3(f)] from the balance of thermal energy densities in the combined *e*-ph system $\rho^{Q}_{\text{e-ph}}$ and in the spin system ρ^{Q}_{s}:

$$\rho^{Q}_{\text{e-ph}}(t) = \rho^{Q}_{\text{e-ph},\infty} + \rho^{Q}_{\text{dyn}} e^{-t/\tau}, \tag{1}$$

$$\rho^{Q}_{\text{sp}}(t) = \rho^{Q}_{\text{sp},0} + \rho^{Q}_{\text{dyn}}(1 - e^{-t/\tau}), \tag{2}$$

$$\rho^{Q}_{\text{laser}} = \rho^{Q}_{\text{e-ph},\infty} + \rho^{Q}_{\text{sp},0} + \rho^{Q}_{\text{dyn}}. \tag{3}$$

In the first 70 ps in Figs. 4(f)–4(h), we may disregard heat transport and assume local conversion of energy $\rho^{Q}_{\text{e-ph}}(t)$ to $\rho^{Q}_{\text{sp}}(t)$ with a coupling time τ. In this model the energy density ρ^{Q}_{laser} imparted by the laser is partially converted to the spin system quasi-instantaneously as $\rho^{Q}_{\text{sp},0}$. ρ^{Q}_{dyn} is transferred from the *e*-ph system to the spins on the timescale τ. $\rho^{Q}_{\text{e-ph},\infty}$ is the heat remaining in the *e*-ph system until heat transport starts to become relevant. The variables $Q_{\text{e-ph}}$, Q_{sp}, and Q_{dyn} have to fulfill energy conservation and approach thermal equilibrium for $t \gg \tau$. The remaining parameter is used to match the amplitude of the signal. The partitioning into only two simulated heat reservoirs is chosen because $\rho^{Q}_{\text{e-ph}}$ and ρ^{Q}_{sp} trigger competing expansive and contractive stresses, respectively. We do not attempt to separate the electron and phonon contributions because this seperation did not improve the fit with the data in the PM phase either. The essential fitting parameter is τ, which we initially assumed coincided with the slow timescale for demagnetization of $\tau_2 = 9$ ps observed by resonant x-ray scattering (RXS) [22]. The fast timescale $\tau_1 = 0.6$ ps is beyond the time resolution we can extract from the lattice dynamics of layers with a thickness on the order of 50 nm. For the modeling we assume an instantaneous coupling of heat energy into the spin system described by $\rho^{Q}_{\text{sp},0}$ in Eq. (2), which mimics τ_1 for the spin disordering observed via RXS, which is attributed to a rapid spin-flip scattering of the optically excited conduction band electrons, enabled by the strong spin-orbit interaction in Ho [22]. Figures 4(f)–4(h) show the excellent agreement achieved simultaneously in the signals from all three layers for $\tau = 12$ ps. Especially, the initial contraction of Ho and the delayed expansion of Nb are very sensitive to variations of τ, as can be seen in the thin lines depicting the simulated signal in Figs. 4(f) and 4(h)

We would like to point out that the intense bipolar strain wave packet launched by the expansion of the capping layer at low temperatures evident from Fig. 4(b) enhances our confidence in the model since it is directly observed in the signal: The short dips in the Y strain [Fig. 4(g)] at 18 ps and in the Nb strain [Fig. 4(h)] at 26 ps indicate the arrival of the narrow compressive part of the bipolar strain pulse, independent of τ. For $\tau = 0$ ps, the maximum in the Nb strain coincides with the minimum observed in the PM phase of Ho. Thus, when all the energy transferred to the spin system arrives there instantaneously, Fig. 4(h) is a nearly perfect mirror image of Fig. 4(e). The increasing delay of the maximum in Nb for increasing τ can be assigned to the delayed NTE stress induced by spin disordering. The blue line in Fig. 3(f) shows once more that the total strain essentially follows the NTE stress profile in Ho (dashed line). Variation of the spatial stress profile of the spin excitation, e.g., to a homogeneous demagnetization profile throughout the layer, has a negligible effect on the Ho signal and does not improve the agreement with the Y and Nb signals.

Finally, we would like to discuss the observation of ultrafast negative stress on the subpicosecond timescale in the context of NTE in general.

NTE requires a specific interaction, where the energy decreases with changes in the volume [33,36]. For Ho the dominant interaction is the exchange interaction J_{exc}, and it was shown earlier that the expansion coefficient $\alpha \sim \partial J_{\text{exc}}/\partial c$ scales with the strain-induced change in the exchange interaction J_{exc} [27,45]. From a statistical physics perspective, the spin entropy $S = R\ln(2J+1)$ must be dominated by the large angular momentum J of the localized $4f$ moments. Hence, the heat energy density ρ^{Q}_{sp} associated with the spin disordering and the concomitant stress $\sigma(t) = \Gamma_{\text{sp}}\rho^{Q}_{\text{sp}}(t)$ is also mainly connected to the localized spins. On the other hand, the RKKY interaction requires the itinerant electrons to mediate the coupling. It is not self-evident if a disordering of the optically excited itinerant electrons alone would be able to explain the full magnitude of the negative stress. In the Ho system, the recent work by Rettig *et al.* [22] confirmed that both types of electrons disorder on the same timescale; however, it will be interesting to test the situation in other systems, such as Gd, where disparate timescales have been observed [46].

VII. CONCLUSION

In conclusion, we have reported that ultrafast laser-induced disordering of the spin system of Ho proceeds on two timescales and triggers NTE via ultrafast stress mediated by

the exchange interaction. On the subpicosecond timescale already nearly half of the negative stress is present, and it fully balances the expansive stress from electrons and phonons. According to the ratio of GCs $\Gamma_{\text{e-ph}}/\Gamma_{\text{sp}} = -0.2$ this balance implies that 20% of the energy absorbed in the Ho layer has excited the spin system. Within $\tau = 12\,\text{ps}$, the fraction of energy in the spin system rises to 40%. If we consider the fact that for the ferromagnetic rare earth Gd, different timescales for disordering the localized and itinerant orbitals have been observed, it is not clear on which timescale the stress should occur. We believe that this study may trigger similar investigations in other systems with NTE since it is not obvious that the thermodynamic relation predicting stress $\sigma = \Gamma\rho^Q$ proportional to the energy density in a subsystem will hold in time-dependent nonequilibrium situations and for any origin of the negative entropy-volume relation required for NTE.

ACKNOWLEDGMENTS

We acknowledge the BMBF for the financial support via 05K16IPA and the DFG via BA 2281/8-1 and BA 2281/11-1. We would like to thank J. Podschwadek for the MBE sample preparation

[1] E. Beaurepaire, J.-C. Merle, A. Daunois, and J.-Y. Bigot, Ultrafast Spin Dynamics in Ferromagnetic Nickel, Phys. Rev. Lett. **76**, 4250 (1996).

[2] J.-Y. Bigot, M. Vomir, and E. Beaurepaire, Coherent ultrafast magnetism induced by femtosecond laser pulses, Nat. Phys. **5**, 515 (2009).

[3] C. Stamm, T. Kachel, N. Pontius, R. Mitzner, T. Quast, K. Holldack, S. Khan, C. Lupulescu, E. F. Aziz, M. Wietstruk, H. A. Dürr, and W. Eberhardt, Femtosecond modification of electron localization and transfer of angular momentum in nickel, Nat. Mater. **6**, 740 (2007).

[4] C. V. Korff Schmising, A. Harpoeth, N. Zhavoronkov, Z. Ansari, C. Aku-Leh, M. Woerner, T. Elsaesser, M. Bargheer, M. Schmidbauer, I. Vrejoiu, D. Hesse, and M. Alexe, Ultrafast magnetostriction and phonon-mediated stress in a photoexcited ferromagnet, Phys. Rev. B **78**, 060404 (2008).

[5] A. H. Reid, X. Shen, P. Maldonado, T. Chase, E. Jal, P. W. Granitzka, K. Carva, R. K. Li, J. Li, L. Wu, T. Vecchione, T. Liu, Z. Chen, D. J. Higley, N. Hartmann, R. Coffee, J. Wu, G. L. Dakovski, W. F. Schlotter, H. Ohldag, Y. K. Takahashi, V. Mehta, O. Hellwig, A. Fry, Y. Zhu, J. Cao, E. E. Fullerton, J. Stöhr, P. M. Oppeneer, X. J. Wang, and H. A. Dürr, Beyond a phenomenological description of magnetostriction, Nat. Commun. **9**, 388 (2018).

[6] G. Malinowski, F. Dalla Longa, J. H. H. Rietjens, P. V. Paluskar, R. Huijink, H. J. M. Swagten, and B. Koopmans, Control of speed and efficiency of ultrafast demagnetization by direct transfer of spin angular momentum, Nat. Phys. **4**, 855 (2008).

[7] D. Rudolf, C. La-O-Vorakiat, M. Battiato, R. Adam, J. M. Shaw, E. Turgut, P. Maldonado, S. Mathias, P. Grychtol, H. T. Nembach, T. J. Silva, M. Aeschlimann, H. C. Kapteyn, M. M. Murnane, C. M. Schneider, and P. M. Oppeneer, Ultrafast magnetization enhancement in metallic multilayers driven by superdiffusive spin current, Nat. Commun. **3**, 1037 (2012).

[8] C. Thomsen, H. T. Grahn, H. J. Maris, and J. Tauc, Surface generation and detection of phonons by picosecond light pulses, Phys. Rev. B **34**, 4129 (1986).

[9] B. Koopmans, G. Malinowski, F. Dalla Longa, D. Steiauf, M. Fähnle, T. Roth, M. Cinchetti, and M. Aeschlimann, Explaining the paradoxical diversity of ultrafast laser-induced demagnetization, Nat. Mater. **9**, 259 (2010).

[10] M. Hofherr, P. Maldonado, O. Schmitt, M. Berritta, U. Bierbrauer, S. Sadashivaiah, A. J. Schellekens, B. Koopmans, D. Steil, M. Cinchetti, B. Stadtmüller, P. M. Oppeneer, S. Mathias, and M. Aeschlimann, Speed and efficiency of femtosecond spin current injection into a nonmagnetic material, Phys. Rev. B **96**, 100403 (2017).

[11] A. V. Kimel, A. Kirilyuk, P. A. Usachev, R. V. Pisarev, A. M. Balbashov, and T. Rasing, Ultrafast non-thermal control of magnetization by instantaneous photomagnetic pulses, Nature (London) **435**, 655 (2005).

[12] J.-W. Kim, M. Vomir, and J.-Y. Bigot, Ultrafast Magnetoacoustics in Nickel Films, Phys. Rev. Lett. **109**, 166601 (2012).

[13] A. Koc, M. Reinhardt, A. von Reppert, M. Rössle, W. Leitenberger, M. Gleich, M. Weinelt, F. Zamponi, and M. Bargheer, Grueneisen-approach for the experimental determination of transient spin and phonon energies from ultrafast x-ray diffraction data: Gadolinium, J. Phys.: Condens. Matter **29**, 264001 (2017).

[14] A. von Reppert, J. Pudell, A. Koc, M. Reinhardt, W. Leitenberger, K. Dumesnil, F. Zamponi, and M. Bargheer, Persistent nonequilibrium dynamics of the thermal energies in the spin and phonon systems of an antiferromagnet, Struct. Dyn. **3**, 054302 (2016).

[15] F. Quirin, M. Vattilana, U. Shymanovich, A.-E. El-Kamhawy, A. Tarasevitch, J. Hohlfeld, D. von der Linde, and K. Sokolowski-Tinten, Structural dynamics in FeRh during a laser-induced metamagnetic phase transition, Phys. Rev. B **85**, 020103 (2012).

[16] X. Wang, S. Nie, J. Li, R. Clinite, M. Wartenbe, M. Martin, W. Liang, and J. Cao, Electronic Grüneisen parameter and thermal expansion in ferromagnetic transition metal, Appl. Phys. Lett. **92**, 121918 (2008).

[17] X. Wang, S. Nie, J. Li, R. Clinite, J. E. Clark, and J. Cao, Temperature dependence of electron-phonon thermalization and its correlation to ultrafast magnetism, Phys. Rev. B **81**, 220301 (2010).

[18] T. Henighan, M. Trigo, S. Bonetti, P. Granitzka, D. Higley, Z. Chen, M. P. Jiang, R. Kukreja, A. Gray, A. H. Reid, E. Jal, M. C. Hoffmann, M. Kozina, S. Song, M. Chollet, D. Zhu, P. F. Xu, J. Jeong, K. Carva, P. Maldonado, P. M. Oppeneer, M. G. Samant, S. S. P. Parkin, D. A. Reis, and H. A. Dürr, Generation mechanism of terahertz coherent acoustic phonons in Fe, Phys. Rev. B **93**, 220301 (2016).

[19] Z. Lin, L. V. Zhigilei, and V. Celli, Electron-phonon coupling and electron heat capacity of metals under conditions of strong electron-phonon nonequilibrium, Phys. Rev. B **77**, 075133 (2008).

[20] P. Maldonado, K. Carva, M. Flammer, and P. M. Oppeneer, Theory of out-of-equilibrium ultrafast relaxation dynamics in metals, Phys. Rev. B **96**, 174439 (2017).

[21] A. von Reppert, L. Willig, J.-E. Pudell, M. Rössle, W. Leitenberger, M. Herzog, F. Ganss, O. Hellwig, and M. Bargheer, Ultrafast laser generated strain in granular and continuous FePt thin films, Appl. Phys. Lett. **113**, 123101 (2018).

[22] L. Rettig, C. Dornes, N. Thielemann-Kühn, N. Pontius, H. Zabel, D. L. Schlagel, T. A. Lograsso, M. Chollet, A. Robert, M. Sikorski, S. Song, J. M. Glownia, C. Schüßler-Langeheine, S. L. Johnson, and U. Staub, Itinerant and Localized Magnetization Dynamics in Antiferromagnetic Ho, Phys. Rev. Lett. **116**, 257202 (2016).

[23] N. Thielemann-Kühn, D. Schick, N. Pontius, C. Trabant, R. Mitzner, K. Holldack, H. Zabel, A. Föhlisch, and C. Schüßler-Langeheine, Ultrafast and Energy-Efficient Quenching of Spin Order: Antiferromagnetism Beats Ferromagnetism, Phys. Rev. Lett. **119**, 197202 (2017).

[24] B. Pfau, S. Schaffert, L. Müller, C. Gutt, A. Al-Shemmary, F. Büttner, R. Delaunay, S. Düsterer, S. Flewett, R. Frömter, J. Geilhufe, E. Guehrs, C. M. Günther, R. Hawaldar, M. Hille, N. Jaouen, A. Kobs, K. Li, J. Mohanty, H. Redlin, W. F. Schlotter, D. Stickler, R. Treusch, B. Vodungbo, M. Kläui, H. P. Oepen, J. Lüning, G. Grübel, and S. Eisebitt, Ultrafast optical demagnetization manipulates nanoscale spin structure in domain walls, Nat. Commun. **3**, 1100 (2012).

[25] M. Doerr, M. Rotter, and A. Lindbaum, Magnetostriction in rare-earth based antiferromagnets, Adv. Phys. **54**, 1 (2005).

[26] M. A. Ruderman and C. Kittel, Indirect exchange coupling of nuclear magnetic moments by conduction electrons, Phys. Rev. **96**, 99 (1954).

[27] F. J. Darnell, Magnetostriction in dysprosium and terbium, Phys. Rev. **132**, 128 (1963).

[28] D. Schick, M. Herzog, A. Bojahr, W. Leitenberger, A. Hertwig, R. Shayduk, and M. Bargheer, Ultrafast lattice response of photoexcited thin films studied by x-ray diffraction, Struct. Dyn. **1**, 064501 (2014).

[29] R. M. van der Veen, O.-H. Kwon, A. Tissot, A. Hauser, and A. H. Zewail, Single-nanoparticle phase transitions visualized by four-dimensional electron microscopy, Nat. Chem. **5**, 395 (2013).

[30] G. Ernst, C. Broholm, G. R. Kowach, and A. P. Ramirez, Phonon density of states and negative thermal expansion in ZrW_2O_8, Nature (London) **396**, 147 (1998).

[31] J. Chen, L. Fan, Y. Ren, Z. Pan, J. Deng, R. Yu, and X. Xing, Unusual Transformation from Strong Negative to Positive Thermal Expansion in $PbTiO_3$-$BiFeO_3$ Perovskite, Phys. Rev. Lett. **110**, 115901 (2013).

[32] S. Khmelevskyi, I. Turek, and P. Mohn, Large Negative Magnetic Contribution to the Thermal Expansion in Iron-Platinum Alloys: Quantitative Theory of the Invar Effect, Phys. Rev. Lett. **91**, 037201 (2003).

[33] T. H. K. Barron, J. G. Collins, and G. K. White, Thermal expansion of solids at low temperatures, Adv. Phys. **29**, 609 (1980).

[34] G. D. Barrera, J. A. O. Bruno, T. H. K. Barron, and N. L. Allan, Negative thermal expansion, J. Phys.: Condens. Matter **17**, R217 (2005).

[35] M. Nicoul, U. Shymanovich, A. Tarasevitch, D. von der Linde, and K. Sokolowski-Tinten, Picosecond acoustic response of a laser-heated gold-film studied with time-resolved x-ray diffraction, Appl. Phys. Lett. **98**, 191902 (2011).

[36] G. K. White, Thermal expansion at low temperatures - V. Dilute alloys of manganese in copper, J. Phys. Chem. Solids **23**, 169 (1962).

[37] G. K. White, Phase transitions and the thermal expansion of holmium, J. Phys.: Condens. Matter **1**, 6987 (1989).

[38] B. C. Gerstein, M. Griffel, L. D. Jennings, R. E. Miller, R. E. Skochdopole, and F. H. Spedding, Heat capacity of holmium from 15 to 300°K, J. Chem. Phys. **27**, 394 (1957).

[39] K. D. Jayasuriya, S. J. Campbell, and A. M. Stewart, Specific heat study of a holmium single crystal, J. Phys. F **15**, 225 (1985).

[40] D. Schick, A. Bojahr, M. Herzog, C. von Korff Schmising, R. Shayduk, W. Leitenberger, P. Gaal, and M. Bargheer, Normalization schemes for ultrafast x-ray diffraction using a table-top laser-driven plasma source, Rev. Sci. Instrum. **83**, 025104 (2012).

[41] See Supplemental Material at http://link.aps.org/supplemental/10.1103/PhysRevB.99.094304 for a video sequence of the temporal evolution of the stress profile and the strain wave in the paramagnetic and antiferromagnetic phases of holmium.

[42] P. Ruello and V. E. Gusev, Physical mechanisms of coherent acoustic phonons generation by ultrafast laser action, Ultrasonics **56**, 21 (2015).

[43] A. I. H. Persson, A. Jarnac, X. Wang, H. Enquist, A. Jurgilaitis, and J. Larsson, Studies of electron diffusion in photo-excited Ni using time-resolved x-ray diffraction, Appl. Phys. Lett. **109**, 203115 (2016).

[44] D. Schick, A. Bojahr, M. Herzog, R. Shayduk, C. von Korff Schmising, and M. Bargheer, UDKM1DSIM - A simulation toolkit for 1D ultrafast dynamics in condensed matter, Comput. Phys. Commun. **185**, 651 (2014).

[45] E. Pytte, Spin-phonon interactions in a Heisenberg ferromagnet, Ann. Phys. (NY) **32**, 377 (1965).

[46] B. Frietsch, J. Bowlan, R. Carley, M. Teichmann, S. Wienholdt, D. Hinzke, U. Nowak, K. Carva, P. M. Oppeneer, and M. Weinelt, Disparate ultrafast dynamics of itinerant and localized magnetic moments in gadolinium metal, Nat. Commun. **6**, 8262 (2015).